



**HAL**  
open science

## **A global probabilistic study of the ocean heat content low-frequency variability: Atmospheric forcing versus oceanic chaos**

Guillaume Sérazin, Alexandre Jaymond, Stephanie Leroux, Thierry Penduff, Laurent Bessières, W. Llovel, Bernard Barnier, Jean-Marc Molines, Laurent Terray

### ► To cite this version:

Guillaume Sérazin, Alexandre Jaymond, Stephanie Leroux, Thierry Penduff, Laurent Bessières, et al.. A global probabilistic study of the ocean heat content low-frequency variability: Atmospheric forcing versus oceanic chaos. *Geophysical Research Letters*, 2017, 44 (11), pp.5580-5589. 10.1002/2017GL073026 . hal-03003527v2

**HAL Id: hal-03003527**

**<https://hal.science/hal-03003527v2>**

Submitted on 8 Apr 2021

**HAL** is a multi-disciplinary open access archive for the deposit and dissemination of scientific research documents, whether they are published or not. The documents may come from teaching and research institutions in France or abroad, or from public or private research centers.

L'archive ouverte pluridisciplinaire **HAL**, est destinée au dépôt et à la diffusion de documents scientifiques de niveau recherche, publiés ou non, émanant des établissements d'enseignement et de recherche français ou étrangers, des laboratoires publics ou privés.

## RESEARCH LETTER

10.1002/2017GL073026

## Key Points:

- The chaotic low-frequency oceanic intrinsic variability (IOV) locally dominates the atmospherically forced oceanic variability
- The IOV explains most of the ocean heat content (OHC) interannual-to-decadal variability in several regions and depth ranges
- The 1980–2010 OHC regional trends cannot be unambiguously attributed to the atmospheric forcing in several regions and depth ranges

## Supporting Information:

- Supporting Information S1

## Correspondence to:

G. Sérazin,  
guillaume.serazin@legos.obs-mip.fr

## Citation:

Sérazin, G., A. Jaymond, S. Leroux, T. Penduff, L. Bessières, W. Llovel, B. Barnier, J.-M. Molines, and L. Terray (2017), A global probabilistic study of the ocean heat content low-frequency variability: Atmospheric forcing versus oceanic chaos, *Geophys. Res. Lett.*, *44*, 5580–5589, doi:10.1002/2017GL073026.



Received 31 JAN 2017

Accepted 5 MAY 2017

Accepted article online 9 MAY 2017

Published online 8 JUN 2017

## A global probabilistic study of the ocean heat content low-frequency variability: Atmospheric forcing versus oceanic chaos

Guillaume Sérazin<sup>1,2</sup> , Alexandre Jaymond<sup>1</sup>, Stéphanie Leroux<sup>1</sup> , Thierry Penduff<sup>1</sup>, Laurent Bessières<sup>2</sup> , William Llovel<sup>2</sup> , Bernard Barnier<sup>1</sup>, Jean-Marc Molines<sup>1</sup>, and Laurent Terray<sup>2</sup> 

<sup>1</sup> Université Grenoble Alpes, CNRS, IRD, IGE, Grenoble, France, <sup>2</sup> CNRS/CERFACS, CECI, Toulouse, France

**Abstract** A global 1/4° ocean/sea ice 50-member ensemble simulation is used to disentangle the low-frequency imprints of the atmospherically forced oceanic variability and of the chaotic intrinsic oceanic variability (IOV) on the large-scale (10° × 10°) ocean heat content (OHC) between 1980 and 2010. The IOV explains most of the interannual-to-decadal large-scale OHC variance over substantial fractions of the global ocean area that increase with depth: 9%, 22%, and 31% in the 0–700 m, 700–2000 m and 2000 m bottom layers, respectively. Such areas concern principally eddy-active regions, mostly found in the Southern Ocean and in western boundary current extensions, and also concern the subtropical gyres at intermediate and deep levels. The oceanic chaos may also induce random multidecadal fluctuations so that large-scale regional OHC trends computed on the 1980–2010 period cannot be unambiguously attributed to the atmospheric forcing in several oceanic basins at various depths. These results are likely to raise detection and attribution issues from real observations.

### 1. Introduction

Greenhouse gases emitted by human activities cause a significant imbalance between incoming and outgoing heat fluxes in the climate system, which results in the current global warming [Intergovernmental Panel on Climate Change, 2013]. Since the 1970s, the global ocean heat content (OHC) has absorbed approximately 93% of this excess heat input into the climate system. Understanding the distribution of this excess heat inside the ocean is a challenging issue given the relatively sparse observational coverage in space and time available [Rhein et al., 2013]. Several studies based on observational data sets have shown that the ocean warming principally occurs above 700 m [Levitus et al., 2009; Ishii and Kimoto, 2009], but intermediate (700–2000 m) [Levitus et al., 2012] and deep (below 2000 m) [Purkey and Johnson, 2010; Kouketsu et al., 2011] layers may also warm, at a slower rate. The horizontal distribution of upper thermal trends is also inhomogeneous: regions such as the North Atlantic subpolar gyre, the tropical southwest Pacific, and the tropical Indian undergo a cooling instead of a warming [see Levitus et al., 2012, Figure S8].

Regional OHC trends computed over half a century result from a subtle balance between the response of the climate system to human activities, the response to natural forcings, and the natural variations spontaneously emerging in the climate system—generally referred to as internal climate variability (hereafter ICV). The contributions of these factors to the globally integrated upper OHC increase since the 1970s are rather well known, but their contributions at regional scale is still a topic of active research [Bindoff et al., 2013]. Attributing regional OHC changes indeed requires a precise estimate of low-frequency (LF) ICV from interannual-to-centennial time scales, currently based on simulations performed with the state-of-the-art climate models. However, such climate models still lack of an accurate representation of the different sources of LF ICV, which reside mainly in atmospheric and oceanic internal dynamics and in air/sea interactions.

In the past, it was thought that the ocean acted as a passive heat reservoir integrating atmospheric fluctuations. This classic view implies that the imprint of the ICV on the OHC is associated either with the oceanic response to atmospheric internal processes (e.g., North Atlantic Oscillation) or with coupled air/sea interactions (e.g., El Niño–Southern Oscillation), but not with ocean-only processes. This paradigm led to the

development of stochastic models [Hasselmann, 1976] in order to explain the characteristics of the sea surface temperature spectrum [Frankignoul and Hasselmann, 1977].

However, recent studies based on eddying Ocean General Circulation Models (OGCMs) have demonstrated that the ocean behaves as a chaotic system, whose internal dynamics may spontaneously generate variability over a wide spatiotemporal spectrum, including basin scales and LF time scales [Penduff *et al.*, 2011; Sérazin *et al.*, 2014; Grégorio *et al.*, 2015]. This so-called intrinsic oceanic variability (hereafter IOV) is not directly forced by the atmospheric variability and originates from oceanic nonlinear processes. Resolving (at least partially) mesoscale turbulence is necessary to simulate a substantial amount of LF IOV (see, for instance, the comparison between the 2° and 1/4° simulations in Penduff *et al.* [2011]). Using an eddy-resolving OGCM, Sérazin *et al.* [2016] showed that in eddying regions, the imprint on sea level of this LF IOV at multidecadal time scales is comparable to the imprint of LF ICV, simulated by current climate models (such as those used in the Coupled Model Intercomparison Project 5), which use laminar ocean components.

The goal of our study is to extend those aforementioned studies of LF IOV, to the whole ocean volume with the LF OHC variability over various depth ranges on the period 1980–2010. We aim at evaluating the respective imprints of the LF IOV and of the atmospheric variability on the OHC, hence assessing the passive oceanic heat reservoir paradigm. In order to simultaneously simulate (and subsequently separate) the forced and intrinsic contributions to the LF OHC variability, we use a novel probabilistic modeling strategy based on a 50-member ensemble of simulations performed over 1960–2015 with a 1/4° eddy-permitting global OGCM [Bessières *et al.*, 2016]. These simulations were driven by the same atmospheric forcing but slightly perturbed in their initial conditions; the chaotic behavior of the eddying ocean dynamics yields 50 different trajectories from which the forced and chaotic ocean variabilities may be disentangled. Ensemble approaches are used in numerical weather prediction and climate science but have been adopted in oceanography only recently.

We focus on two climate-related ranges of time scales: interannual-to-decadal ( $2 \text{ years} < T < 15 \text{ years}$ ) and multidecadal ( $T > 30 \text{ years}$ ). Two main questions are addressed in this paper: (1) In which regions does the interannual-to-decadal chaotic IOV of regional OHC dominate its atmospherically forced counterpart? (2) Where can the OHC trends over 1980–2010 be unambiguously attributed to atmospheric forcing? Where can the chaotic IOV hamper the detection of forced OHC trends over 1980–2010?

We investigate these questions within three depth ranges (0–700 m, 700–2000 m, and 2000–6000 m) consistently with the coverage and evolution of in situ observing systems (see Abraham *et al.* [2013] for a review). The development of expendable bathythermograph (XBT) observing systems has provided a reasonable spatial coverage of the upper 300 m since the 1970s and of the upper 700 m since the 1990s. The Argo profiling float [Roemmich *et al.*, 2009] has extended this coverage to 2000 m depth since 2001, with a global coverage reached in 2005. Future oceanic observation such as Deep Argo [Johnson *et al.*, 2015] would extend the Argo sampling to the poorly probed deep ocean (i.e., the 2000–6000 m layer), which represents 52% of the total oceanic volume [Abraham *et al.*, 2013]. Both past and future measurements might be impacted by the oceanic “noise” (chaotic IOV), which would complicate the interpretation of the observed OHC variability in relation to the atmospheric variability.

## 2. Data and Methods

### 2.1. Model Simulations

We use the probabilistic version [Bessières *et al.*, 2016] of the NEMO ocean model (Nucleus for European Model of the Ocean, [Madec, 2008]), implemented on the global ocean at 1/4° horizontal resolution with 75 vertical levels. Each simulation is forced by the Drakkar Forcing Set (DFS) version 5.2 [Dussin and Barnier, 2013], based on the ERA40/ERA-Interim reanalyses. The model settings (e.g., advection scheme and diffusion coefficients) are similar to the 1/4° simulations performed with the ORCA025 configuration and used in previous studies to characterize the LF IOV [i.e., Penduff *et al.*, 2011; Grégorio *et al.*, 2015; Sérazin *et al.*, 2016].

Our integration strategy consists of a 21 year spin-up followed by a 56-member ensemble simulation, both driven by the 1958–2015 DFS5.2 forcing. One model member is started from rest in 1958 and spun-up until the end of 1977. A modified forcing, linearly interpolated from 1 January 1978 to 31 January 1958, is then applied for 1 month to smoothly bring the oceanic state back to February 1958. The spin-up is resumed between 1 February 1958 and 31 December 1959 under nominal DFS5.2 forcing. The 50 members are initialized by this spun-up state on 1 January 1960 and integrated under DFS5.2 forcing until the end of 2015. A stochastic

parameterization that slightly perturbs the density field [Brankart, 2013] is activated in 1960 to trigger the ensemble dispersion and then switched off at the end of 1960. Ensemble statistics are computed after the integration, from which the LF forced variability and IOV are calculated. Because the atmospheric reanalyses used in DFS5.2 do not include any interannual variability in the buoyancy fluxes before 1980 and because we had data storage issues after 2010, we hereafter focus our analyses on the 1980–2010 period.

In addition to this ensemble simulation, we performed a one-member 327 year climatological simulation forced each year by the mean seasonal atmospheric cycle derived from DFS5.2. This experiment is close to that used in previous studies of LF IOV [e.g., Penduff *et al.*, 2011; Sérazin *et al.*, 2014] and is used here to estimate and compensate the model drift.

## 2.2. Ocean Heat Content Computation

The local OHC is computed at each time step  $t$ , from each of the 50 ensemble members (denoted by  $n$ ) by integrating the three-dimensional  $(x, y, z)$  monthly temperature fields between depths  $z_1$  and  $z_2$ :

$$\text{OHC}(n, t, x, y) = \rho_0 c_p \int_{z_1}^{z_2} T(n, t, x, y, z) dz, \quad (1)$$

where the density of seawater  $\rho_0 = 1020 \text{ kg m}^{-3}$  and the calorific capacity per unit mass  $c_p = 4000 \text{ J kg}^{-1} \text{ K}^{-1}$  are taken constant. Note that the OHC is defined here per unit area so that data sets at different grid resolutions may be compared. The local OHC is computed for layers 0–700 m, 700–2000 m, and 2000–6000 m, which cover the ocean from the surface to the bottom, and averaged over successive years. OHC fields are then spatially smoothed using a low-pass bidimensional Lanczos filter [Duchon, 1979] in order to remove structures smaller than  $10^\circ \times 10^\circ$  and focus on larger scale. The same processing is applied to the climatological simulation.

## 2.3. Estimating the Interannual-To-Decadal OHC Variability

In order to limit biases in the computation of interannual-to-decadal OHC standard deviations, we remove all time scales longer than about 15 years (hence the trends) from the 50-member yearly OHC fields in the three layers, using the nonparametric LOcal regrESSion (LOESS) method [see Cleveland and Devlin, 1988; Sérazin *et al.*, 2014; Grégorio *et al.*, 2015]. The subsequent high-passed OHC time series thus contain periods ranging from 2 years to about 15 years for each member. An example of such filtered 50-member time series is given in Figure S1 in the supporting information. The intensity of the interannual-to-decadal forced OHC variability  $\sigma_F$  is then estimated from the temporal unbiased standard deviation of the ensemble mean OHC time series:

$$\sigma_F = \sqrt{\frac{1}{Y-1} \sum_{i=1}^Y (\langle \text{OHC} \rangle - \overline{\langle \text{OHC} \rangle})^2}, \quad (2)$$

where  $\langle x \rangle$  and  $\overline{x_i}$  denotes, respectively, the ensemble and temporal means of  $x_i$ .  $Y$  is the total number of years (i.e., 31). The intensity of the interannual-to-decadal IOV  $\sigma_I$ , induced by chaotic oceanic motions, is estimated by time averaging the OHC ensemble unbiased variance:

$$\sigma_I = \sqrt{\frac{1}{N-1} \sum_{i=1}^N (\text{OHC}_i - \langle \text{OHC} \rangle)^2}, \quad (3)$$

where  $N$  is the total number of ensemble member (i.e., 50). The ratio of these standard deviations yields the signal-to-noise ratio  $\text{SNR} = \sigma_F / \sigma_I$ . This SNR may be used to quantify the ability to detect a forced signal, i.e., induced by the atmospheric variability, among the ambient noise generated by chaotic oceanic motions, i.e., the IOV. The intensity of the total variability of OHC is simply estimated by  $\sigma_T = \sqrt{\sigma_F^2 + \sigma_I^2}$ .

## 2.4. Computing the 1980–2010 OHC Trends

To estimate the local impact of IOV on OHC at multidecadal time scales, we compute linear trends from raw monthly time series over the 1980–2010 period (for each member and each layer). We reduce biases due to the model drift by computing the corresponding local OHC linear trends from the climatological simulation (shown in Figure S2) and by subtracting these trends to the 50-member ensemble of OHC trends. After this correction, the ensemble mean is thus an estimator of regional OHC trends induced by the atmospheric forcing, and the ensemble standard deviation is an estimator of the uncertainty induced by the oceanic chaos.

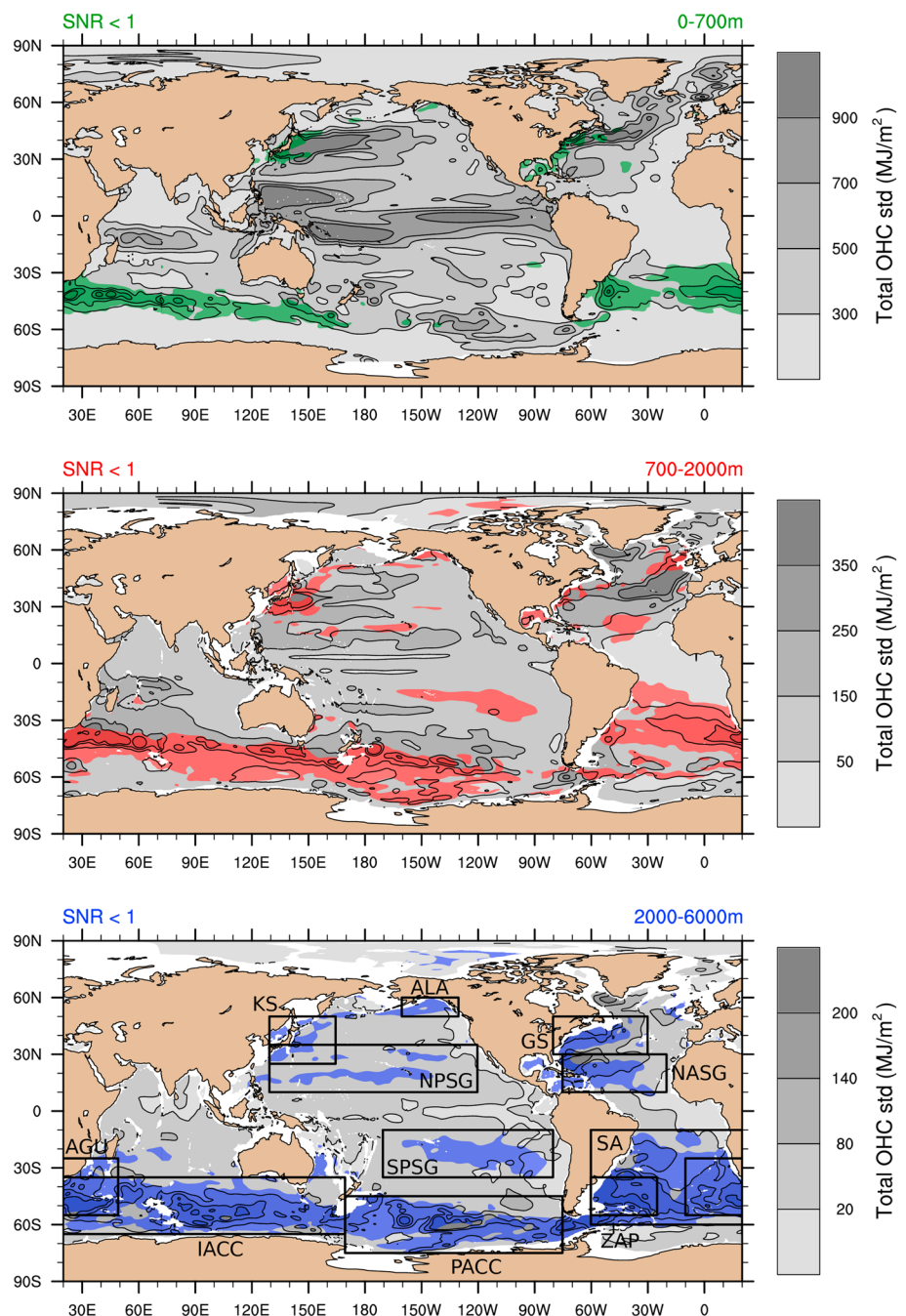


**Figure 1.** Total (forced + chaotic) interannual-to-decadal OHC standard deviation (SD, gray shading) at scales larger than  $10^\circ \times 10^\circ$ , shown in layers (top) 0–700 m, (middle) 700–2000 m, and (bottom) 2000–6000 m. Color shading indicates regions where the chaotic SD exceeds the forced SD. Figure 2 is focused on the OHC integrated horizontally over the regions shown in Figure 1 (bottom).

### 3. Interannual-to-Decadal OHC Variability

In this section, the term variability will refer to interannual-to-decadal time scales. We first focus on total ( $\sigma_T$ ) OHC variability maps and associated signal-to-noise ratios (SNR) in the three layers (Figure 1). The corresponding maps for intrinsic ( $\sigma_I$ ) and forced ( $\sigma_F$ ) OHC variability are shown in Figures S3 and S4, respectively.

In the 0–700 m layer (top), the total OHC variability is large in eddy-active western boundary currents (WBCs), in particular, in the Gulf Stream and the Kuroshio, and all along the Antarctic Circumpolar Current (ACC).

The chaotic IOV dominates the forced variability ( $\text{SNR} < 1$ , green shading) throughout most of the ACC aside from the Pacific sector and in small areas of the Gulf Stream and of the Kuroshio. The Zapiola anticyclone, associated with the Brazil-Malvinas Confluence, and the Agulhas leakage are also characterized by large OHC variability, which is almost everywhere dominated by chaotic IOV. The tropical Pacific and Indian Oceans exhibit substantial OHC variability, probably linked to El Niño–Southern Oscillation (ENSO) and the Indian Ocean Dipole, respectively. The OHC variability in these intertropical regions is however mainly forced by the atmospheric variability ( $\text{SNR} > 1$ ). Overall, the chaotic IOV exceeds the forced interannual-to-decadal OHC variability over 9% of the global ocean area in the 0–700 m layer.

In the 700–2000 m layer (Figure 1, middle), the total OHC variability remains large in eddy-active regions with a distribution that differs from the upper layer: it is shifted toward the eastern part of the North Atlantic and shrinks closer to Japan in the North Pacific. The midlatitude OHC variability is mostly forced by the atmosphere ( $\text{SNR} > 1$ ) in the Northern Hemisphere, although the IOV predominates in more regions than above 700 m ( $\text{SNR} < 1$ , red shading): Pacific WBC system and China Sea, Gulf of Alaska, Rockall Plateau, and Gulf of Mexico. At high latitudes, the Labrador Sea has large total OHC variability, mainly induced by the atmospheric forcing ( $\text{SNR} > 1$ ) and probably related to the deep convection occurring in this region. The OHC variability is weaker at lower latitudes, except in the Indian Ocean, and is mostly forced by the atmospheric variability everywhere between 10°S and 10°N. The chaotic IOV, however, locally dominates the forced OHC variability along the equatorward flanks of the subtropical gyres in the Atlantic and Pacific Oceans. The total OHC variability is clearly dominated by chaotic IOV throughout most of the South Atlantic subtropics, and almost everywhere along the ACC. Overall, the chaotic IOV dominates the forced interannual-to-decadal OHC variability over 22% of the 700–2000 m layer area, i.e., substantially more than above 700 m.

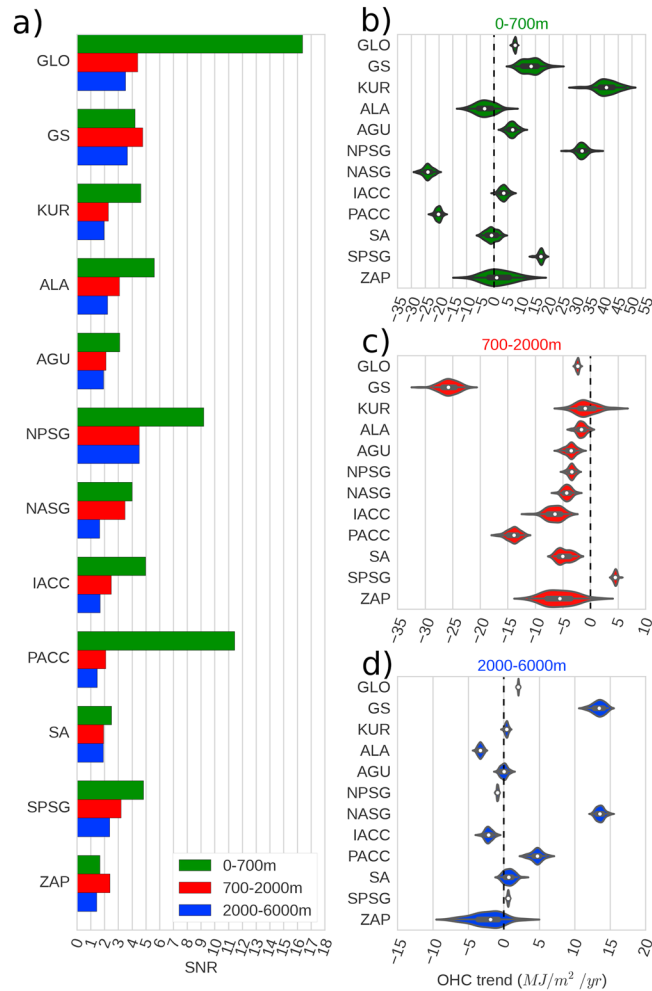
In the 2000–6000 m layer (Figure 1, bottom), the total OHC variability becomes weak in the Kuroshio but remains substantial in the northwestern subtropical Atlantic, in the Southern Ocean, and in the South Atlantic midlatitudes. In most of these regions and along the equatorward flanks of subtropical gyres, most of the OHC variability comes from the chaotic IOV ( $\text{SNR} < 1$ , blue shading). The same conclusion holds for the China sea and the Gulf of Alaska. In contrast, the total OHC variability maximum simulated in the Labrador Sea at all depths is mostly controlled by the atmospheric forcing ( $\text{SNR} > 1$ ). The relative imprint of IOV has thus further increased downward: the chaotic IOV exceeds the forced interannual-to-decadal OHC variability over 31% of the 2000–6000 m layer area.

Figure 2a provides diagnostics at larger scales: it shows SNRs computed from three-dimensional integrals of OHC in the three layers and over the regions denoted by black boxes in Figure 1 (bottom) (exact coordinates are given in Table S5). This panel first confirms that the interannual-to-decadal SNR decreases monotonically with depth for the globally integrated OHC (GLO), as well as in most of the regions mentioned above. This panel also demonstrates that chaotic IOV still has a substantial imprint ( $1.5 < \text{SNR} < 2.5$ ) on the variability of the OHC integrated over very wide regions, such as the whole subtropical South Atlantic (SA, all depths), the whole Indian and Pacific sectors of the Southern Ocean (IACC and PACC, below 700 m).

In summary, the interannual-to-decadal OHC variability is mostly forced by the atmospheric variability in tropical regions and in the Labrador Sea, within all depth ranges. The chaotic IOV, however, exceeds the atmospherically forced OHC variability in several regions of the world ocean: regions of intense mesoscale activity such as the WBCs and the ACC and also the Pacific and Atlantic subtropical gyres. The relative contribution of IOV to the total OHC variability tends to increase with depth as the imprint of the atmospheric variability decreases: (1) regions where the interannual-to-decadal IOV exceeds its forced counterpart represent 9%, 22%, and 31% of the global ocean area in the 0–700 m, 700–2000 m, and 2000–6000 m layers, respectively and (2) the impact of IOV on the OHC integrated over very wide regions also increases with depth and remains very substantial.

#### 4. Multidecadal OHC Variability: 31 Year Trends

Figures 2b–2d show the probability density functions (PDFs) of 1980–2010 OHC trends integrated over the same layers and regions as above and deduced from the 50 ensemble members. The 0–700 m layer globally (GLO) warms at an estimated (mean) rate of  $7.5 \text{ MJ yr}^{-1} \cdot \text{m}^{-2}$  ( $0.24 \text{ W m}^{-2}$ ). This forced trend falls into the different observational estimates made over the period 1980–2012 [see Abraham *et al.*, 2013, Figure 14]. The forcing induces a global cooling in the 700–2000 m layer at a rate of  $-2.4 \text{ MJ yr}^{-1} \cdot \text{m}^{-2}$  ( $-0.08 \text{ W m}^{-2}$ ), which is not consistent with the observational study of Levitus *et al.* [2012] that rather suggests that this intermediate layer



**Figure 2.** (a) Interannual-to-decadal SNR ( $\sigma_F/\sigma_I$ , see text) of the OHC integrated over three depth ranges (0–700 m in green, 700–2000 m in red, and 2000–6000 m in blue) and over 12 regions: Global Ocean (GLO), Gulf Stream (GS), Kuroshio (KUR), Gulf of Alaska (ALA), Agulhas current (AGU), North Pacific Subtropical Gyre (NPSG), North Atlantic Subtropical Gyre (NASG), Indian ACC (IACC), Pacific ACC (PACC), South Atlantic (SA), South Pacific Subtropical Gyre (SPSG), and CONF (Brazil-Malvinas Confluence). The 1980–2010 linear trends of the OHC integrated over the regions shown in Figure 1 and over (b) the 0–700 m layer, (c) the 700–2000 m layer, and (d) the 2000–6000 m layer; color shading shows ensemble PDFs, white dots ensemble medians, and thick bars the range between the 25th and 75th percentiles.

warmed from 1955 to 2010. The forcing eventually warms the 2000–6000 m layer at a rate of  $2.0 \text{ MJ yr}^{-1} \text{ m}^{-2}$  ( $0.06 \text{ W m}^{-2}$ ), which is hardly comparable with the actual deep ocean due to the lack of observations.

These globally integrated OHC trends are barely affected by the oceanic chaos as the PDF spreads are marginal in each of the layers. This result is consistent with the idea that intrinsic fluctuations of mesoscale and regional circulations randomly redistribute heat over the horizontal without modifying the global OHC.

Results are different at regional scale. In the 0–700 m layer, certain regions warm (e.g., KUR, GS, and NPSG) while others cool (e.g., NASG and PACC) due to the forcing (white dots, median) over this 31 year period. In the 700–2000 m layer, most regions cool, except the South Pacific subtropical gyre (SPSG). The largest forced cooling rates are found in the Gulf Stream (GS) and in the Pacific ACC (PACC). In most regions, however, the PDFs of OHC trends exhibit a substantial ensemble spread induced by multidecadal IOV ( $\geq 5 \text{ MJ/m}^2/\text{yr}$  in the 0–700 m layer,  $\geq 2 \text{ MJ/m}^2/\text{yr}$  in the 700–2000 m layer), except in the South Pacific subtropical gyre (SPSG) and the Pacific ACC (PACC).

The Zapiola (ZAP) region in our simulation is particularly impacted by multidecadal IOV, which yields a large spread in OHC trends in the three layers. Ensemble PDFs of simulated OHC trends in this region overlap the

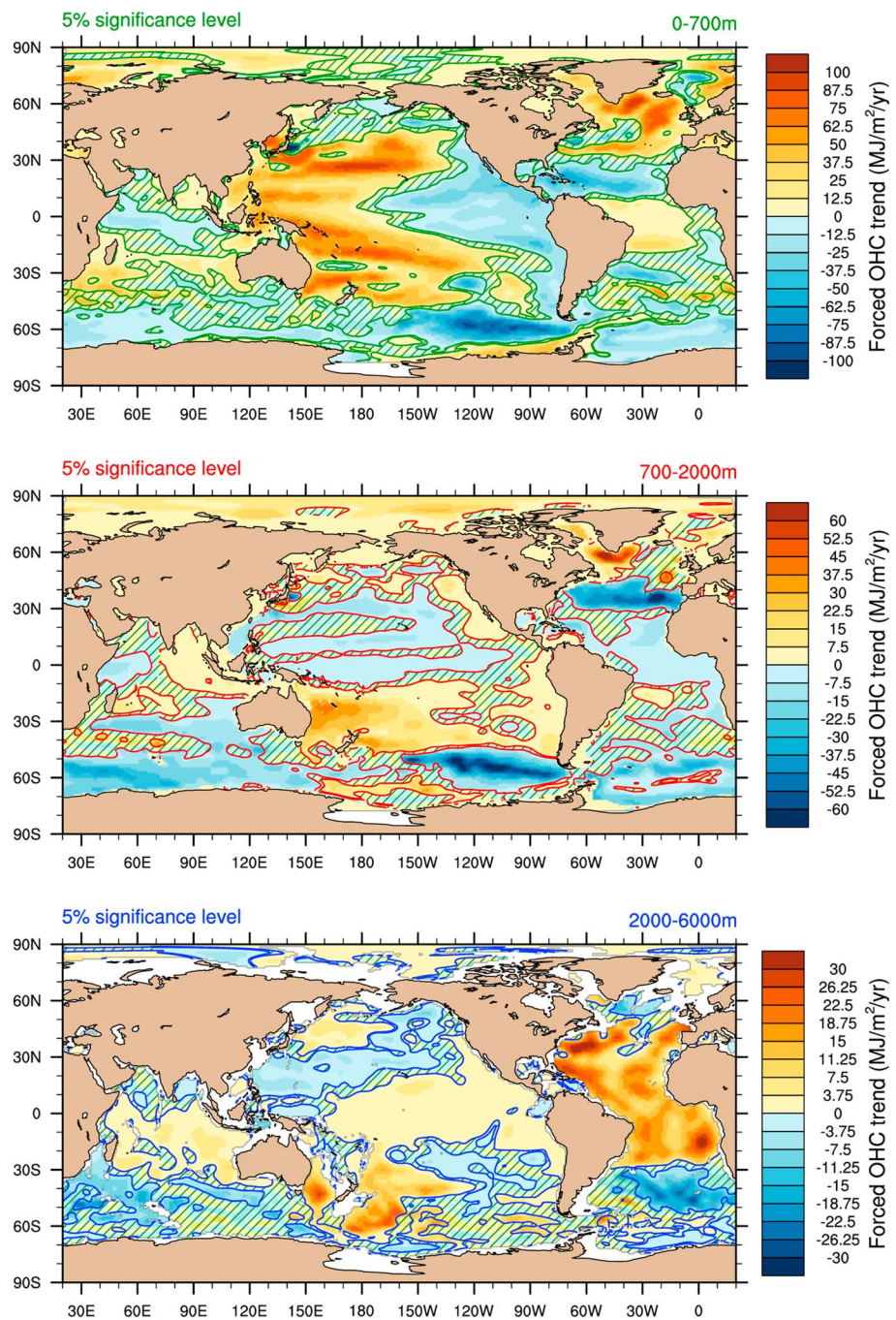


**Figure 3.** Colors: atmospherically forced (ensemble mean) trend of the regional OHC over the period 1980–010 in layers (top) 0–00 m, (middle) 700–000 m, and (bottom) 2000–000 m. In hatched regions, the trend cannot be unambiguously attributed to the atmospheric forcing (95% confidence interval).

zero line at all depths and in other regions in certain layers (e.g., ALA above 2000 m, SA above 700 m, KUR in the 700–000 m layer, and AGU in the 2000–000 m layer). In these regions, such overlaps imply that it is not possible to assert the sign of the forced OHC trend in a particular member. The potential implications of these findings for observational studies are discussed in section 5.

Interestingly, ensemble PDFs are also somewhat different from Gaussian distributions in the Gulf Stream (GS), Kuroshio (KS), and South Atlantic (SA) regions. However, to be able to test the significance of regional cooling or warming in connection with the atmospheric forcing during 1980–2010, we assume that random trends due to internal ocean dynamics (IOV) are normally distributed with a zero mean and with a standard deviation



estimated from the 50-member ensemble spread. We thus test the forced (ensemble mean) OHC trend against the null hypothesis that the trend is zero. When this null hypothesis is rejected, we may state that the trend is not significantly forced by the atmosphere but is rather randomly induced by the oceanic chaos. We chose a 95% confidence interval, i.e., two standard deviations. We apply this test on the regional maps of forced OHC trends; results are shown in Figure 3 where nonsignificant trends are highlighted with hatched contours.

In the Pacific, the 0–700 m layer (Figure 3, top) warms in the west from 1980 to 2010, cools in the east and in the Southern Ocean. This pattern is consistent with the observed interdecadal modulation of ENSO, i.e., a transition between positive and negative phases of the Pacific Decadal Oscillation (PDO) and the Indian Pacific Oscillation (IPO) between 1980 and 2010 [Chen and Wallace, 2015]. During this period, the zonal thermocline tilt becomes steeper and yields an increased heat storage in the western part of the basin. Our statistical test shows that over most of the basin, the simulated 31 year trend may indeed be unambiguously attributed to the atmospheric forcing.

In the hatched regions, however, the ensemble mean OHC trends become small enough to fall into the random uncertainty induced by multidecadal IOV and may not be unambiguously attributed to the atmospheric forcing. Our results suggest that this concerns many regions of the global ocean: most of the subpolar North Pacific and South Atlantic, a large part of the Indian Ocean, a wide region south of Australia, the Beaufort Sea, the Gulf Stream region and a zonal band across the subtropical North Atlantic, etc. Most of these results corroborate our conclusions about regional trends (Figure 2b).

The 700–2000 m layer (Figure 3, middle) exhibits a large cooling in the Pacific part of the Southern Ocean as well as a large warming east of Australia, similar to OHC trends found in the upper layer. In these regions, OHC trends may be significantly attributed to the atmospheric forcing and are probably the extension of the upper layer imprint of the PDO and IPO down to the middepth ocean. In the North Atlantic, the atmospheric forcing unambiguously warms the Labrador Sea and cools the subtropical gyre.

Again, our results suggest that middepth OHC trends cannot be unambiguously attributed to atmospheric causes because of substantial random imprints of multidecadal IOV in several regions (red hatched contours): regions surrounding the large patterns mentioned above, regions close to those hatched in the 0–00 layer (e.g., South Atlantic, North Pacific subpolar gyre, Agulhas Return Current, and Arabian Sea), and additional regions (e.g., central North Pacific west of Hawaii and eastern North Atlantic).

In the deep 2000–6000 m layer (Figure 3, bottom), our results suggest that the atmosphere does force large warming trends over a wide part of the Atlantic Ocean and in the southwestern Pacific. These warming trends are consistent with a deep ocean heat uptake that stores a large fraction of the excess heat from anthropogenic warming in the Atlantic and in the Southern Ocean [Chen and Tung, 2014; Liu et al., 2016]. In our model, a substantial cooling trend also occurs in the midlatitude South Atlantic as well as weaker trends over other regions (e.g., most of the North Pacific). At these depths, it is not possible to unambiguously attribute the 31 year OHC trends to atmospheric causes in most regions south of about 30°S (and in other regions too), where multidecadal IOV yields relatively large ensemble spreads.

In summary, our analyses show that multidecadal IOV does hamper the unambiguous attribution of regional OHC 31 year trends to the atmospheric forcing over large regions of the global ocean at various depths, such as in the South Atlantic, the Southern Ocean, and the Arabian Sea.

## 5. Conclusion and Discussion

The analysis of an eddy-permitting ensemble simulation shows that over most of the global ocean, the atmospheric variability is the main driver of the LF regional OHC variability at interannual-to-decadal (section 3) and multidecadal (section 4) time scales. However, the simulated oceanic turbulence leads to the spontaneous emergence of chaotic IOV, which has a significant imprint on LF OHC variability while being uncorrelated with the atmospheric variability. At interannual-to-decadal time scales, this chaotic IOV exceeds the atmospherically forced OHC variability in many areas of the Southern Ocean, in turbulent western boundary currents, but also in more quiescent regions. The relative importance of the chaotic IOV over its forced counterpart tends to increase with depth: the OHC variability is mostly chaotic over one third of the deep ocean area. At multidecadal time scales, the chaotic IOV also projects on regional 31 year OHC trends, forbidding the unambiguous attribution of these trends to atmospheric causes in many regions (large parts of the Southern Ocean, Arabian Sea, etc.)

The randomness of the intrinsic signal raises important issues for the detection, attribution, and interpretation of regional fluctuations in certain regions of the ocean, in the context of climate change [Bindoff *et al.*, 2013]. First, the chaotic contribution of the oceanic turbulence to the LF OHC variability highlights the limitations of the passive heat reservoir paradigm in several regions of the global ocean. As a consequence, the classic null hypothesis of an atmospherically forced red noise spectrum [Frankignoul and Hasselmann, 1977], commonly used in climate-related studies, may not be well suited to test the significance of spectral peaks in eddy-active regions. We argue that further work is needed to update this current null hypothesis in order to take into account the LF intrinsic noise produced by the turbulent ocean.

Second, this eddy-induced noise is not taken into account in the construction of time-varying three-dimensional temperature fields from ocean observations [e.g., Ishii and Kimoto, 2009; Levitus *et al.*, 2012] nor in its interpretation for climate monitoring. Our results indeed suggest that individual observations, such as XBT or Argo temperature profiles, may capture the imprint of chaotic IOV as well as long-term atmospherically induced climate change signals. The impact of the local IOV-induced random uncertainties on temperature reconstructions has not been addressed in this study, but it would be possible and perhaps valuable to provide the observational community with error bars deduced the ensemble spread after collocation on each of the temperature profiles. Figure S5 shows that these local uncertainties are not negligible and are even larger than those shown for large-scale ( $10^\circ \times 10^\circ$ ) OHC variability in Figure 1. Identifying precisely these chaotic uncertainties is an important issue to address since future oceanic observations will sample the deep ocean, where oceanic IOV may be relatively important compared to the atmospherically forced signal.

The novel approach used in our study, which estimates LF IOV from ensemble statistics, gives consistent results with the previous studies that use only one climatological simulation to estimate the IOV. In particular, regions where the chaotic IOV substantially imprints the OHC are associated with regions where the IOV imprint on sea level was shown to be substantial at interannual-to-decadal [Penduff *et al.*, 2011; Sérazin *et al.*, 2014] and multidecadal time scales [Sérazin *et al.*, 2016]. Those OHC intrinsic fluctuations might be the result of random heat redistributions by oceanic turbulence and could substantially contribute to intrinsic sea level fluctuations through the thermosteric component. Grégorio *et al.* [2015] also showed that intrinsic processes may explain about 25% of the Atlantic meridional heat transport LF variability at  $34^\circ\text{S}$ , i.e., in a region where it also explains most of the OHC variability. The link between the dynamical and thermal imprints of the chaotic IOV still needs to be clarified.

Disentangling properly the forced and chaotic global ocean variabilities requires large ocean-only simulation ensembles in the eddying regime, which are only possible at eddy-permitting resolution today. However, long climatological simulations showed that the  $1/4^\circ$  resolution captures many features of the IOV simulated at  $1/12^\circ$  [Grégorio *et al.*, 2015], albeit with a weaker imprint on sea level [Sérazin *et al.*, 2014].

In any case, the present results suggest that the LF oceanic chaos may, in turn, have atmospheric impacts in future climate projections, which are currently implemented with  $1/4^\circ$  ocean models. The chaotic IOV imprint on OHC is indeed strong in the regions (Gulf Stream, Kuroshio, Agulhas, etc.) where air-sea heat fluxes are largest in nature and could influence the climate in such experiments. Verifying this hypothesis lies beyond the scope of the present study, which nevertheless suggests an increase in the complexity and richness in climate projections with turbulent oceans.

## References

- Abraham, J. P., *et al.* (2013), A review of global ocean temperature observations: Implications for ocean heat content estimates and climate change, *Rev. Geophys.*, *51*, 450–483, doi:10.1002/rog.20022.
- Bessières, L., S. Leroux, J.-M. Brankart, J.-M. Molines, M.-P. Moine, P.-A. Bouttier, T. Penduff, L. Terray, B. Barnier, and G. Sérazin (2016), Development of a probabilistic ocean modelling system based on NEMO 3.5: Application at eddying resolution, *Geosci. Model Dev.*, *10*, 1091–1106, doi:10.5194/gmd-2016-174.
- Bindoff, N., *et al.* (2013), Detection and attribution of climate Change: From global to regional, in *Climate Change 2013: The Physical Science Basis. Contribution of Working Group I to the Fifth Assessment Report of the Intergovernmental Panel on Climate Change*, edited by T. Stocker *et al.*, pp. 867–952, Cambridge Univ. Press, Cambridge, U. K., and New York.
- Brankart, J.-M. (2013), Impact of uncertainties in the horizontal density gradient upon low resolution global ocean modelling, *Ocean Modell.*, *66*, 64–76, doi:10.1016/j.ocemod.2013.02.004.
- Chen, X., and K.-K. Tung (2014), Varying planetary heat sink led to global-warming slowdown and acceleration, *Science*, *345*(6199), 897–903, doi:10.1126/science.1254937.
- Chen, X., and J. M. Wallace (2015), ENSO-like variability: 1900–2013, *J. Clim.*, *28*(24), 9623–9641, doi:10.1175/JCLI-D-15-0322.1.
- Cleveland, W. S., and S. J. Devlin (1988), Locally weighted regression: An approach to regression analysis by local fitting, *J. Am. Stat. Assoc.*, *83*(403), 596–610, doi:10.2307/2289282.

## Acknowledgments

This work is mainly a contribution to the OCCIPUT project (see <http://meom-group.github.io/projects/occiput/>), which is supported by ANR through contract ANR-13-BS06-0007-01. The model outputs used for this study can be made available upon request by contacting thierry.penduff@univ-grenoble-alpes.fr. We acknowledge that the results of this research have been achieved using the PRACE Research Infrastructure resource CURIE based in France at TGCC. The support of the TGCC-CCRT hotline from CEA, France, to the technical work is gratefully acknowledged. The diagnostics presented in this study were performed at TGCC under allocations granted by GENCI. This work also benefited from many interactions with the DRAKKAR ocean modeling consortium, with the SANGOMA and CHAOCEAN projects. DRAKKAR is the International Coordination Network (GDRI) established between CNRS, NOCS, GEOMAR in Kiel, and IFREMER. SANGOMA is funded by the European Community's Seventh Framework Programme FP7/2007-2013 under grant agreement 283580. CHAOCEAN is funded by CNES through the Ocean Surface Topography Science Team (OST/ST). The authors also thank the NEMO System Team and Yann Meurdesoif for interesting discussions about the development of the probabilistic version of NEMO. G.S., A.J., S.L., and L.B. are supported by ANR, T.P., B.B., and J.M.M. are supported by CNRS, L.T. is supported by CERFACS, and W.L. is supported by CNES.

- Duchon, C. (1979), Lanczos filtering in one and 2 dimensions, *J. Appl. Meteorol.*, *18*(8), 1016–1022, doi:10.1175/1520-0450(1979)018<1016:LFOAT>2.0.CO;2.
- Dussin, R., and B. Barnier, (2013), The making of DF55.1, Drakkar Project Rep., Grenoble, France.
- Frankignoul, C., and K. Hasselmann (1977), Stochastic climate models, Part II Application to sea-surface temperature anomalies and thermocline variability, *Tellus*, *29*(4), 289–305, doi:10.1111/j.2153-3490.1977.tb00740.x.
- Grégorio, S., T. Penduff, G. Sérazin, J.-M. Molines, B. Barnier, and J. Hirschi (2015), Intrinsic variability of the Atlantic meridional overturning circulation at interannual-to-multidecadal timescales, *J. Phys. Oceanogr.*, *45*, 1929–1946, doi:10.1175/JPO-D-14-0163.1.
- Hasselmann, K. (1976), Stochastic climate models Part I. Theory, *Tellus*, *28*(6), 473–485, doi:10.1111/j.2153-3490.1976.tb00696.x.
- Intergovernmental Panel on Climate Change (2013), *Climate Change 2013: The Physical Science Basis. Contribution of Working Group I to the Fifth Assessment Report of the Intergovernmental Panel on Climate Change*, Cambridge Univ. Press, Cambridge, U. K., and New York.
- Ishii, M., and M. Kimoto (2009), Reevaluation of historical ocean heat content variations with time-varying XBT and MBT depth bias corrections, *J. Oceanogr.*, *65*(3), 287–299, doi:10.1007/s10872-009-0027-7.
- Johnson, G. C., J. M. Lyman, and S. G. Purkey (2015), Informing deep argo array design using argo and full-depth hydrographic section data, *J. Atmos. Oceanic Technol.*, *32*(11), 2187–2198, doi:10.1175/JTECH-D-15-0139.1.
- Kouketsu, S., et al. (2011), Deep ocean heat content changes estimated from observation and reanalysis product and their influence on sea level change, *J. Geophys. Res.*, *116*, C03012, doi:10.1029/2010JC006464.
- Levitus, S., J. I. Antonov, T. P. Boyer, R. A. Locarnini, H. E. Garcia, and A. V. Mishonov (2009), Global ocean heat content 1955–2008 in light of recently revealed instrumentation problems, *Geophys. Res. Lett.*, *36*, L07608, doi:10.1029/2008GL037155.
- Levitus, S., et al. (2012), World ocean heat content and thermosteric sea level change (0–2000 m), 1955–2010: World ocean heat content, *Geophys. Res. Lett.*, *39*, L10603, doi:10.1029/2012GL051106.
- Liu, W., S.-P. Xie, and J. Lu (2016), Tracking ocean heat uptake during the surface warming hiatus, *Nat. Commun.*, *7*, 10926, doi:10.1038/ncomms10926.
- Madec, G., (2008), NEMO ocean engine, Note du Pole de modélisation 27, Institut Pierre-Simon Laplace, IPSL, France.
- Penduff, T., M. Juza, B. Barnier, J. Zika, W. K. Dewar, A.-M. Treguier, J.-M. Molines, and N. Audiffren (2011), Sea level expression of intrinsic and forced ocean variabilities at interannual time scales, *J. Clim.*, *24*(21), 5652–5670, doi:10.1175/JCLI-D-11-00077.1.
- Purkey, S. G., and G. C. Johnson (2010), Warming of global abyssal and deep southern ocean waters between the 1990s and 2000s: Contributions to global heat and sea level rise budgets, *J. Clim.*, *23*(23), 6336–6351, doi:10.1175/2010JCLI3682.1.
- Rhein, M., et al. (2013), Observations: Ocean, in *Climate Change 2013: The Physical Science Basis. Contribution of Working Group I to the Fifth Assessment Report of the Intergovernmental Panel on Climate Change*, edited by T. Stocker et al., pp. 255–316, Cambridge Univ. Press, Cambridge, U. K., and New York.
- Roemmich, D., G. Johnson, S. Riser, R. Davis, J. Gilson, W. B. Owens, S. Garzoli, C. Schmid, and M. Ignaszewski (2009), The argo program: Observing the global oceans with profiling floats, *Oceanography*, *22*(2), 34–43, doi:10.5670/oceanog.2009.36.
- Sérazin, G., T. Penduff, S. Grégorio, B. Barnier, J.-M. Molines, and L. Terray (2014), Intrinsic variability of sea level from global ocean simulations: Spatiotemporal scales, *J. Clim.*, *28*(10), 4279–4292, doi:10.1175/JCLI-D-14-00554.1.
- Sérazin, G., B. Meyssignac, T. Penduff, L. Terray, B. Barnier, and J.-M. Molines (2016), Quantifying uncertainties on regional sea level change induced by multidecadal intrinsic oceanic variability, *Geophys. Res. Lett.*, *43*, 8151–8159, doi:10.1002/2016GL069273.